EAI Endorsed Transactions
on Energy Web
Research Article EAI.EU

Research on Predictive Control Energy Management Strategy for Composite Electric Ship Based on Power Forecasting

Haotian Chen[1,*] and Xixia Huang[2]

[1]Institute of Logistics Science and Engineering, Shanghai Maritime University, Shanghai 201306, China
[2]Key Lab of Transport Industry of Marine Technology and Control Engineering, Shanghai Maritime University, Shanghai 201306, China

Abstract

INTRODUCTION: A proposed solution is presented to address the issue of rising energy loss resulting from inaccurate power prediction in the predictive energy management strategy for composite electric power electric ship.
OBJECTIVES: The solution involves the development of a power prediction model that integrates Archimedes' algorithm, optimized variational modal decomposition, and BiLSTM.
METHODS: Within the framework of Model Predictive Control, this predictive model is utilized for power forecasting, transforming the global optimization problem into one of optimizing the power output distribution among power sources within the predictive time domain, then the optimization objective is to minimize the energy loss of the composite electric power system, and a dynamic programming algorithm is employed to solve the optimization problem within the forecast time domain.
RESULTS: The simulation findings demonstrate a significant enhancement in the forecast accuracy of the power prediction model introduced in this study, with a 52.61% improvement compared to the AOA-BiLSTM power prediction model. Concurrently, the energy management strategy utilizing the prediction model proposed in this research shows a 1.02% reduction in energy loss compared to the prediction model control strategy based on AOA-BiLSTM, and a 15.8% reduction in energy loss compared to the ruler-based strategy.
CONCLUSION: The simulation findings demonstrate a significant enhancement in the forecast accuracy of the power prediction model introduced in this study.

Keywords: composite electric power system; ship; energy management; model predictive control; power prediction; neural network; variational modal decomposition

Received on 20 December 2023, accepted on 26 March 2024, published on 03 April 2024

doi: 10.4108/ew.4653

*Corresponding author. Email: haotianch@outlook.com

Full Name	Abbreviations
Energy management strategy	EMS
Model predictive control	MPC
Long and short-term memory	LSTM
Bidirectional LSTM	BiLSTM
Variational mode decomposition	VMD
Archimedes optimization algorithm	AOA
Ultracapacitor	UC
State of charge	SOC
Intrinsic mode functions	IMF

1. Introduction

Composite electric power system is among the principal directions in the development of current new-energy ships. The coupling of various power sources endows these systems with pronounced nonlinear characteristics, complicating the distribution of energy. A critical issue demanding resolution in their energy management strategy (EMS) is how to realize the efficient operation of each power source within these composite electric systems, thereby reducing system energy consumption and energy loss.

Currently, the ruler-based EMS is extensively employed in practical engineering applications. For example, Han achieved the goal of improving system efficiency by setting a ruler-based EMS based on determining the threshold value for a hybrid ship composed of fuel cells and batteries [1]. Unlike the deterministic ruler-based strategy proposed by Han, Halima proposed a fuzzy ruler-based EMS to optimize emissions for parallel hybrid electric vehicles. The control of different power supply operation modes and the control of battery charging states are realized by means of the affiliation function [2]. The ruler-based EMS is characterized by its ease of implementation and real-time performance. However, the determination of the threshold value in this strategy relies on engineering experience and actual calibration results, leading to limited adaptability to varying working conditions. The working conditions of a ship encompass its various operational modes, such as cruising and mooring. This article examines these working conditions as indicators of power value and variability, with a specific emphasis on the management strategy derived from each power source. Consequently, the system experiences significant energy losses, making the implementation of optimal control measures a difficult task [3]. To solve these problems caused by ruler-based EMS, scholars have studied optimal EMS. While dynamic programming (DP) can achieve optimal control in global optimization strategies [4], it is important to note that it requires knowledge of future working conditions and involves a significant computational burden. As a result, DP can only be optimized offline to serve as a reference for online strategies, rather than being directly implemented for online control [5]. The challenge in EMS research lies in achieving a balance between the control effect of the control strategy and real-time considerations.

For the above reasons, some researchers proposed EMS focused on instantaneous optimization and aims to transform the energy management problem into a problem of finding extreme values for the objective function [6]. By simplifying the control object and optimizing the solution method, the computational load is reduced [7]. Consequently, this approach exhibits potential for practical implementation in engineering applications. One of the strategies for minimizing energy consumption is the equivalent energy consumption minimization strategy. This strategy aims to reduce the energy consumption of each power source to a unified energy consumption index by introducing an equivalence factor [8]. For instance, Ge proposed the design of a fuzzy logic controller that adaptively improves the equivalent consumption minimization control strategy. This controller adjusts the equivalent factor in real time, optimizes the operating points of the fuel cell system, and then achieves the goal of improving the system efficiency [9]. By doing so, the global optimization problem is transformed into the problem of minimizing instantaneous energy consumption at each sampling moment. The effectiveness of this strategy heavily relies on the appropriate setting of the equivalence factor. Despite Ge's efforts to improve this issue using fuzzy logic controllers, the adaptive equivalent consumption minimization strategy suggested by Ge heavily depends on a fuzzy logic control approach. The empirical nature of the fuzzy rules and affiliation functions in this strategy can result in heightened energy consumption and loss, as well as exacerbate the challenges associated with designing the equivalent consumption minimization strategy [10]. To overcome this drawback, the researchers proposed another optimization-type EMS called model predictive control (MPC). The MPC transforms the problem of globally optimizing power allocation into a localized power optimization problem within a specified prediction time domain. This approach employs an optimization algorithm to optimize power allocation within the prediction time domain. The effectiveness of this control strategy relies on the accuracy of power prediction, making power prediction the central and challenging aspect of the MPC strategy. Hence, the prediction model of power is the fundamental and challenging aspect of the MPC method.

Numerous studies have been conducted by scholars to forecast short-term power in the future. Linear regression is a conventional approach that has been shown to yield superior prediction outcomes for linear problems [11]. However, its applicability is limited when it comes to addressing nonlinear difficulties. The advancement of intelligent technology has led to the emergence of modern intelligent methods, including neural networks, which possess enhanced processing capabilities in addressing nonlinear problems. Examples of such methods include BP neural network [12] and long and short-term memory (LSTM) neural network [13]. Hu employed a BP neural network for power prediction; nevertheless, it leads to underfitting because of its lack of generalization capability [14]. Yan employed the LSTM neural network to forecast power, successfully addressing the issue of gradient explosion and vanishing that occur during the training phase [15]. While according to Zhao's article, bidirectional LSTM (BiLSTM) outperforms a single LSTM structural model in terms of data feature extraction efficiency and performance. Zhao used an estimate method for short-term demand of electricity based on WOA-BiLSTM in order to use the BiLSTM neural network layer for bidirectional time series feature learning [16]. Furthermore, Putz have enhanced the predictive accuracy by augmenting the network's depth [17], and Houran employed optimization algorithms to maximize the hyper-parameters [18]. These efforts have resulted in a certain degree of improvement in accuracy.

The working conditions of ships are intricate, and the power demands vary significantly under different scenarios. such as mooring, cruising, and power positioning. These variations are complex, unpredictable, and lack regularity. Consequently, accurately predicting future power requirements becomes more challenging due to the increased difficulty in anticipating these changes. The aforementioned study primarily concentrates on enhancing the model's nonlinear fitting capability from a modelling perspective, while disregarding the impact of power non-stationarity on prediction accuracy. Besides, although BiLSTM has the advantages of being able to learn time series features and solve the gradient vanishing problem, setting its appropriate internal parameters is a difficult problem. Consequently, the extent to which prediction accuracy is improved remains limited.

In response to the above problems with current research, some novel contributions to this research are proposed:

1. It improves the precision of subsequent power prediction by utilizing variational mode decomposition (VMD) to extract potential data patterns from working condition data and decrease the non-stationarity of the power series.

2. The proposed method involves optimizing the key parameters of VMD and BiLSTM. This research introduces an optimization approach that employs the Archimedes optimization algorithm (AOA) to improve power prediction accuracy.

The proposed power prediction model, consists of two primary components: the decomposition model and the prediction model. Unlike conventional direct prediction models that depend on power data, this study suggests an approach utilizing the AOA to optimize the parameters of VMD. The goal is to decompose the power sequence into multiple subsequences to reduce the inherent non-smoothness of the power sequence. The power prediction is subsequently achieved via the BiLSTM model optimized by AOA. Following this, a predictive EMS is developed, based on the outcomes of power prediction, within the model predictive control strategy architecture. This strategy involves conducting rolling optimization of the power allocation problem in the predictive time domain, aiming ultimately to minimize system energy loss.

Hence, this article commences by introducing the composite power system model that incorporates a battery and ultracapacitor (UC). Subsequently, an examination of the power combination prediction model is conducted, and the DP solver in MPC, which is proposed in this paper, is implemented on its foundation. Subsequently, simulation experiments are executed within the MATBLAB software. Comparative experiments are conducted utilizing both a ruler-based approach and a global optimization approach.

2. Composite Electric Power System Model

The composite electric power system consists of battery and UC as dual power sources [19]. In this system, the battery serves as the primary power source, while the UC functions as the auxiliary power source. The structure of this system is depicted in Figure 1.

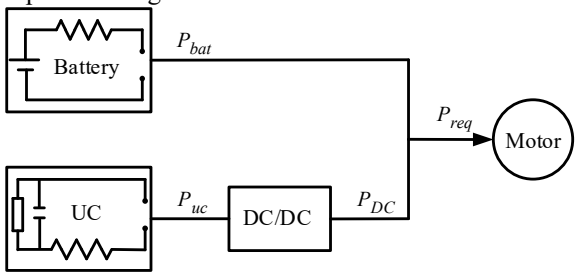

Figure 1. Composite electric power supply system structure

During navigation, the correlation between the power source and the motor's power requirement can be expressed using the following equations.

$$\begin{cases} P_{req} = P_{bat} + P_{uc} \\ P_{uc} = P_{DC} \cdot \eta_{DC}^{\,sign(P_{uc})} \end{cases} \tag{1}$$

$$sign(x) = \begin{cases} 1 & if\ x > 0 \\ 0 & if\ x = 0 \\ -1 & if\ x < 0 \end{cases} \tag{2}$$

P_{req}, P_{uc} and P_{bat} stands for the required power of the motor, the power of the UC and the power of the battery, respectively, In equations (1) and (2). While η_{DC} is the DC/DC efficiency, P_{DC} is the power of DC/DC near the motor.

Four types of ship propulsion working modes can be distinguished based on power consumption. Table 1 describes these modes and their power distribution.

Table 1. The working mode and power relationship of electric ships

Working Mode	Power Management Strategy
Battery Driven	$P_{req} = P_{bat},\ P_{uc} = 0$
Ultracapacitor Driven	$P_{req} = P_{uc},\ P_{bat} = 0$
Hybrid Driven	$P_{req} = P_{bat} + P_{uc},\ P_{uc} > 0$
Charging	$P_{req} = P_{bat} + P_{uc},\ P_{uc} < 0$

2.1. Battery Model

Equations (3) and (4) display the battery pack current and SOC calculation expressions, and the corresponding internal resistance model is established.

$$I_{bat} = \frac{U_{oc\_bat} - \sqrt{U_{oc\_bat}^2 - 4R_{bat} \cdot P_{bat}}}{2R_{bat}} \tag{3}$$

$$SOC_{bat} = SOC_{bat\_init} - \frac{\int_0^t I_{bat} dt}{Q_{bat}} \tag{4}$$

The battery current, open circuit voltage, internal resistance, initial SOC, and rated capacity are represented respectively by the variables I_{bat}, U_{oc_bat}, R_{bat}, SOC_{bat_init}, and Q_{bat} in equations (3) and (4). Figure 2 illustrates the link between battery SOC and U_{oc_bat}, R_{bat}.

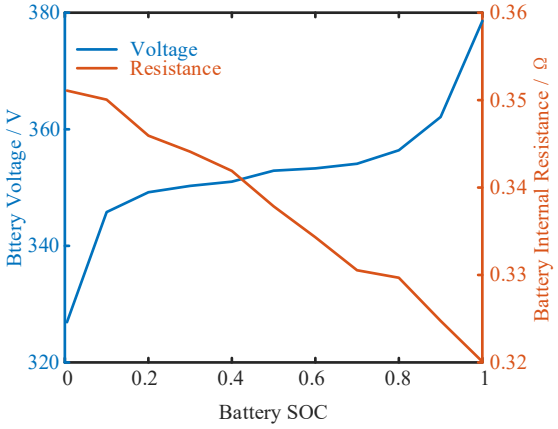

Figure 2. Relationship between battery SOC, open circuit voltage and internal resistance

2.2. Ultracapacitor Model

The UC can be represented by an internal resistance model, which is analogous to that of the battery. The current and SOC of the UC can be calculated using the following equations (5) and (6).

$$I_{uc} = \frac{U_{oc\_uc} - \sqrt{U_{oc\_uc}^2 - 4R_{uc} \cdot P_{uc}}}{2R_{uc}} \tag{5}$$

$$SOC_{uc} = \frac{U_{oc\_uc}}{U_{uc\_max}} \tag{6}$$

The UC current, open circuit voltage, maximum voltage, and internal resistance are represented by the variables I_{uc}, U_{oc_uc}, U_{oc_max}, and R_{uc} in equations (5) and (6), respectively. Figure 3 illustrates the relationship between U_{oc_uc}, R_{uc}, and UC SOC.

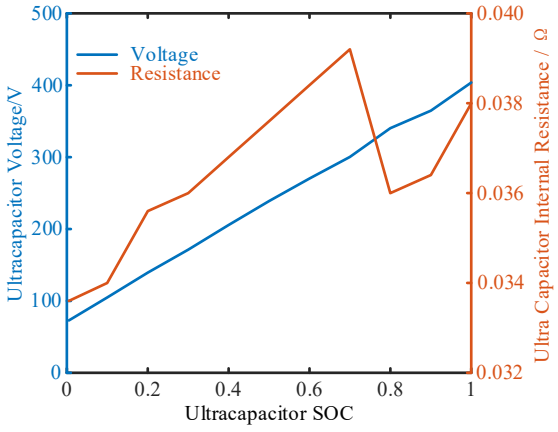

Figure 3. Relationship between UC SOC, open circuit voltage and internal resistance

2.3. Bidirectional DC/DC converter model

This paper solely examines the DC/DC's operational efficiency, ignoring the intricate internal mechanism changes. Figure 4 illustrates how power affects its efficiency.

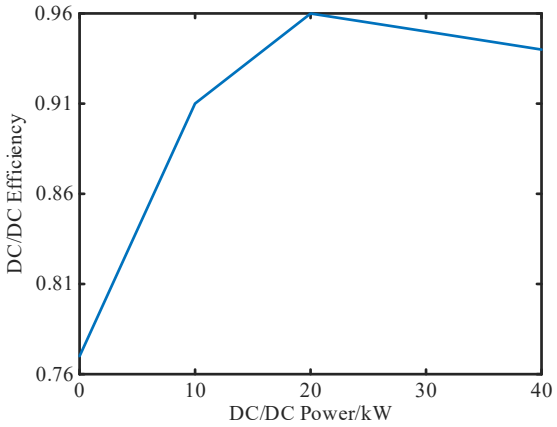

Figure 4. DC/DC efficiency and power relationship curve

3. Power Combination Prediction Model

3.1. Construction of Power Combination Prediction Model

Due to the non-stationarity of ship operational condition time series, a single prediction model is insufficient in terms of prediction accuracy. Although its mapping ability can be enhanced through optimization algorithms, the improvement is limited and the prediction accuracy remains unsatisfactory, impacting the effectiveness of control outcomes. Therefore, to enhance the accuracy of power prediction, a combined prediction model based on AOA-optimized VMD and BiLSTM is proposed, as illustrated in Figure 5. The power prediction process of this model is as follows:

1. Decomposition: Initially, the power series undergoes decomposition through the AOA-VMD algorithm into N distinct modal components. A comprehensive explanation of this algorithm is available in Section 3.5;
2. Prediction: Subsequently, normalization is applied to each modal component, followed by the establishment of individual AOA-BiLSTM prediction models. The AOA algorithm is instrumental in optimizing the hyperparameters associated with the BiLSTM neural network, extensively detailed in Section 3.6;
3. Fusion: Finally, the predictive outputs from each component are aggregated and synthesized to formulate the comprehensive power prediction outcome.

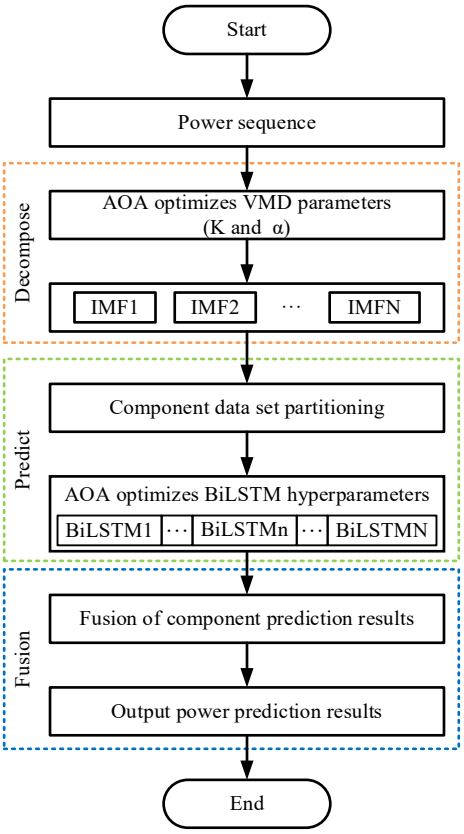

Figure 5. Power prediction flow chart

3.2. VMD Feature Extraction Algorithm

VMD is a decomposition method that breaks down signals into a series of simple modal components [20]. The process of power prediction in this model is illustrated through the following steps:

1. Decomposing the original signal into several modal components. This is based on the principle that the sum of the decomposed components should equal the original signal, aiming to minimize bandwidth. The calculation formula is as shown in Equation (7):

$$\begin{cases} \min\limits_{\{u_k\},\{\omega_k\}} \left\{ \sum\limits_{k=1}^{K} \left\| \partial_t \left[\left(\delta(t) + \dfrac{j}{\pi t} \right) * u_k(t) \right] e^{-j\omega_t} \right\|_2^2 \right. \\ s.t. \sum\limits_{k=1}^{K} u_k(t) = f(t) \end{cases} \tag{7}$$

where K represents the total number of decompositions performed, ∂_t is utilized to denote a gradient operation and the symbol $*$ is a convolution operation and $\delta(t)$ refers to the pulse signal. $\{u_k\}$ and $\{\omega_k\}$ are modal and center frequency sets, respectively. Lastly, $f(t)$ symbolizes the original signal;

2. In order to solve the problem of vulnerability to constraints, the Lagrange multiplication operator $\lambda(t)$ and the multiplication factor α are introduced, and the calculation method is shown in equation (8);

$$\begin{aligned} &L\left(\{u_k\},\{\omega_k\},\ \lambda\right) = \\ &\alpha \sum_{k=1}^{K} \left\| \partial_t \left[\left(\delta(t) + \frac{j}{\pi t} \right) * u_k(t) \right] e^{-j\omega_t} \right\|_2^2 + \\ &\left\| f(t) - \sum_{k=1}^{K} u_k(t) \right\|_2^2 + \left\langle \lambda(t), f(t) - \sum_{k=1}^{K} u_k(t) \right\rangle \end{aligned} \tag{8}$$

Where α represents the penalty factor. The penalty factor of VMD plays a role in balancing the signal-to-noise ratio and decomposition accuracy in the decomposition process.

3. Each modal component and centre frequency are calculated and the expression is shown in equation (9):

$$\begin{cases} \hat{u}^{n+1}(\omega) = \dfrac{\hat{f}(\omega) - \sum\limits_{i \neq k} \hat{u}_i(\omega) + \dfrac{\hat{\lambda}(\omega)}{2}}{1 + 2\alpha(\omega - \omega_k)^2} \\ \omega_k^{n+1} = \dfrac{\int_0^{\infty} \omega \left| \hat{u}_k(\omega) \right|^2 d\omega}{\int_0^{\infty} \left| \hat{u}_k(\omega) \right|^2 d\omega} \end{cases} \tag{9}$$

where $\hat{u}^{n+1}(\omega)$ and ω_k^{n+1} are the k-th modal component and centre frequency of centre frequency ω at the (n+1)-th iteration, respectively.

3.3. BiLSTM Model

In addition to addressing the issues of gradient eruption and vanishing, LSTM possesses the selective memory capability, which confers additional benefits when processing lengthy time sequences. It is composed of an output gate o_t, an updating gate i_t, and a forgetfulness gate f_t. The schematic representation of the structure is illustrated in Figure 6.

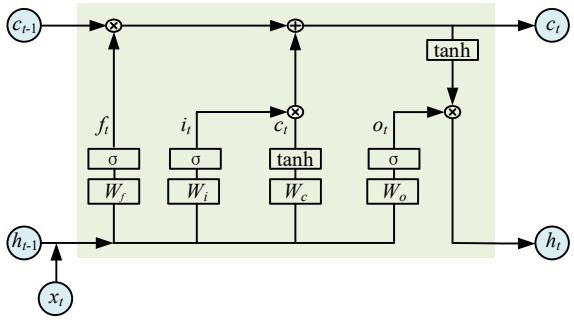

Figure 6. LSTM structure diagram

In Figure 6, x_t is the input at moment t, $W_{f,i,c,o}$ and $b_{f,i,c,o}$ are the weights and biases of the corresponding gates, respectively. σ is the Sigmoid activation function, c_t is the cell state at moment t. c_{t-1} and h_{t-1} are the cell state and the hidden state at the moment t-1. As can be seen from Figure 6, the output h_t of LSTM are jointly determined by x_t,

c_{t-1} and h_{t-1}. First, the f_t, i_t and o_t can be calculated from x_t and c_{t-1}. Then, the h_t can be calculated based on the output result of c_t and gate. The LSTM computation process is shown in equations (10) to (14).

$$f_t = \sigma\left(W_f \times \left[h_{t-1}, x_t\right] + b_f\right) \tag{10}$$

$$i_t = \sigma\left(W_i \times \left[h_{t-1}, x_t\right] + b_f\right) \tag{11}$$

$$c_t = f_t \cdot c_{t-1} + i_t \cdot \tanh\left(W_c \times \left[h_{t-1}, x_t\right] + b_c\right) \tag{12}$$

$$o_t = \sigma\left(W_o \times \left[h_{t-1}, x_t\right] + b_o\right) \tag{13}$$

$$h_t = o_t \cdot \tanh\left(c_t\right) \tag{14}$$

The structure diagram of BiLSTM is presented in Figure 7. It comprises a bidirectional LSTM, which differs from the unidirectional LSTM in that it learns from both the forward and backward sequences. By leveraging the bidirectional structure, BiLSTM is able to effectively utilize the data and enhance the accuracy of predictions, as compared to the sole utilization of forward-to-backward learning in LSTM.

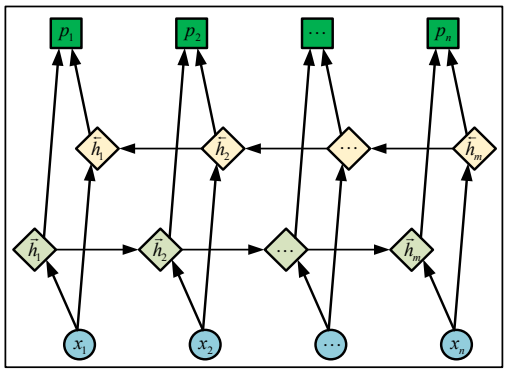

Figure 7. BiLSTM structure diagram

3.4. AOA algorithm

After determining the decomposition and prediction models, it is necessary to further ascertain the key parameters of these models. For instance, in the VMD model, choosing parameters such as the number of decomposition layers and penalty coefficients, and in the BiLSTM model, selecting the number of hidden nodes and the learning rate significantly influences prediction accuracy. Relying solely on experience to determine these parameters can compromise the models' generalizability and reliability. Therefore, this paper employs the AOA method to optimize the key parameters of both the VMD and BiLSTM models.

The AOA algorithm is derived from Archimedes' principle and shares similarities with other optimization algorithms. Like its counterparts, the AOA algorithm encompasses an initiation phase, a search phase, and a position updating process. The precise processes of the algorithm are outlined as following steps:

Initialization

$$\begin{cases} x_i = lb_i + rand \cdot \left(ub_i - lb_i\right) \\ acc_i = lb_i + rand \cdot \left(ub_i - lb_i\right) \\ den_i = rand_i \\ vol_i = rand_i \end{cases} \tag{15}$$

where x_i and acc_i are the position and acceleration of the i-th object; den_i and vol_i are the density and volume of the first object; ub_i and lb_i are the upper and lower bounds of the search space; and *rand* is a random number in the range of [0,1].

The position x_{best}, the optimal density den_{best}, the optimal volume vol_{best} and the optimal acceleration acc_{best} of the object with optimal adaptation are obtained according to the adaptation evaluation function.

4. Density and volume update

$$\begin{cases} den_i^{t+1} = den_i^t + rand \times \left(den_{best} - den_i^t\right) \\ vol_i^{t+1} = vol_i^t + rand \times \left(vol_{best} - vol_i^t\right) \end{cases} \tag{16}$$

5. Calculation of the transfer operator T and the density factor d

Following the occurrence of the collision between the objects, a process of progressive equilibration takes place, resulting in the cessation of further collisions. This equilibration is determined through the calculation of variables T and d, as expressed in equation (17):

$$\begin{cases} T = \exp\left(\dfrac{t - t_{\max}}{t_{\max}}\right) \\ d^{t+1} = T - \dfrac{t}{t_{\max}} \end{cases} \tag{17}$$

6. Development and search

If $T > 0.5$, there is no collision between the objects for development and the acceleration is updated using the following equation (18):

$$acc_i^{t+1} = \frac{den_{best} + vol_{best} \cdot acc_{best}}{den_i^{t+1} + vol_i^{t+1}} \tag{18}$$

A collision between objects takes place when $T \leq 0.5$. In such a case, a search is executed, a random object is chosen, and the acceleration is modified utilizing equation (19):

$$acc_i^{t+1} = \frac{den_{mr} + vol_{mr} \cdot acc_{mr}}{den_i^{t+1} + vol_i^{t+1}} \tag{19}$$

where den_{mr}, vol_{mr}, and acc_{mr} are the density, volume, and acceleration of a randomly selected object.

Equation (20) can be obtained by normalizing equations (18) and (19):

$$acc_{in}^{t+1} = u \times \frac{acc_i^{t+1} - acc_{\min}}{acc_{\max} - acc_{\min}} + l \tag{20}$$

where acc_{in}^{t+1} is the result of acceleration normalization; u and l are set constants; acc_{max} and acc_{min} are the maximum and minimum values of acceleration.

7. Object position update

If $T > 0.5$, the updated expression for the position of the i-th object in the development phase is:

$$x_i^{t+1} = x_{best}^t + F \cdot C_1 \cdot rand \cdot acc_{in}^{t+1} \cdot d \cdot \left(D \cdot x_{best} - x_i^t \right) \quad (21)$$

If $T \le 0.5$, the updated expression for the position of the i-th object in the development phase is:

$$x_i^{t+1} = x_i^t + C_2 \cdot rand \cdot acc_{in}^{t+1} \cdot d \cdot \left(x_{rand} - x_i^t \right) \quad (22)$$

where x_{rand} is the random object position; C_1 and C_2 are constants; D is defined as the product of constants C_3 and T; and F is the position update flag with the expression:

$$F = \begin{cases} 1 & if\ P \le 0.5 \\ -1 & else \end{cases} \quad (23)$$

In equation (23), there is $P = 2 \times rand - C_4$ and C_4 is constant.

3.5. AOA-optimized VMD

In the process of signal decomposition using VMD, it is imperative to predefine certain parameters, including the modal number K, penalty factor α, and time step. Among these parameters, K and α significantly impact the outcomes of the decomposition. However, setting these parameters manually poses challenges in ensuring the accuracy of the decomposition results and achieving optimal decomposition efficacy. Hence, this research suggests utilizing the envelope entropy as the adaptation function in order to decrease it, while employing AOA to determine the ideal values of K and α.

This work examines the concept of envelope entropy (E_p) as a measure of the sparsity of a signal. Additionally, it explores the relationship between the amount of heavy information contained in the intrinsic mode functions (IMF) component after decomposition and the inverse proportionality to E_p. The inverse relationship between the size of E_p and the amount of information it contains is evident. Conversely, an increase in noise is observed as E_p increases. This relationship can be expressed as the following equation (24):

$$\begin{cases} E_p = -\sum_{i=1}^{N} \varepsilon(i) \lg \varepsilon(i) \\ \varepsilon(i) = \dfrac{a(i)}{\sum_{i=1}^{N} a(i)} \end{cases} \quad (24)$$

where $a(i)$ is the envelope signal of K components after Hilbert demodulation; $\varepsilon(i)$ is the form of normalized probability distribution of $a(i)$; N is the number of sampling points.

The merit seeking process is shown in the Figure 8 below with the following steps:

1. Initialize parameters such as object position in AOA algorithm, range of K and α;
2. Power decomposition using VMD and calculation of adaptation values;
3. Update various individual positions using AOA algorithms and calculate and update minimum adjustment values;
4. Repeat steps 2 and 3 until the iterative convergence condition is satisfied or the maximum number of iterations is reached and then output the optimal K and α parameters;
5. Execute power decomposition while setting the K and alpha of the VMD to the optimal K and α parameter values obtained in step 4.

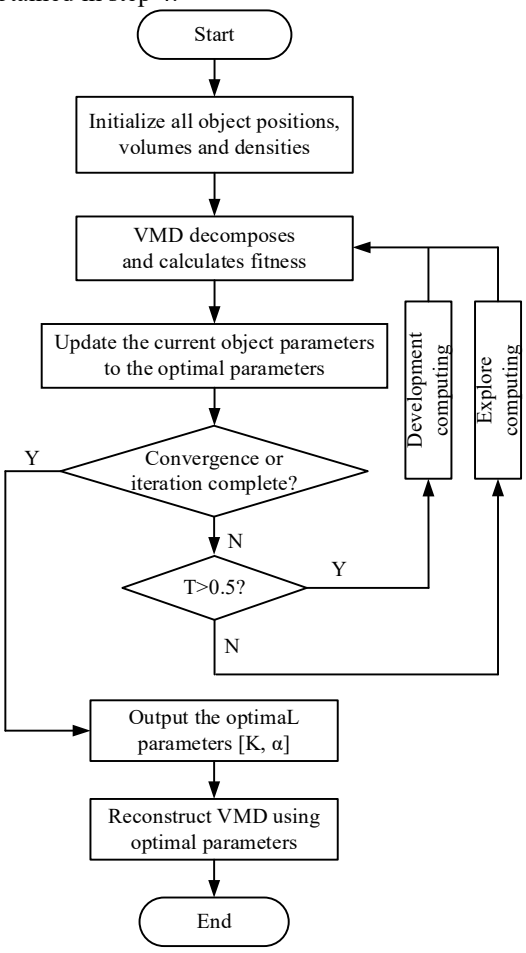

Figure 8. AOA-optimized VMD flow chart

3.6. AOA-optimized BiLSTM

Since BiLSTM parameters have a direct impact on the precision of prediction outcomes, their optimization is required. This paper describes the utilization of AOA to optimize the learning rate, L2 regularization coefficients, and number of hidden nodes in a BiLSTM network. The detailed procedure is illustrated in Figure 9, and it consists of the following steps:

1. Initialize the object location of the AOA algorithm and the ranges of the three selected hyperparameters;
2. Employ the mean square error as the adaptation value when training the BiLSTM model and calculating the adaptation value;
3. Implementing the AOA algorithm to modify the positions of multiple individuals while simultaneously computing and revising the minimum fitness value;
4. Proceed with steps 2 and 3 iteratively until the iterative convergence condition is fulfilled or until the maximum

number of iterations is completed and the optimal hyperparameters are output;

5. Train the BiLSTM model using the middle optimization parameter of BiLSTM as the optimal parameter output from step 4.

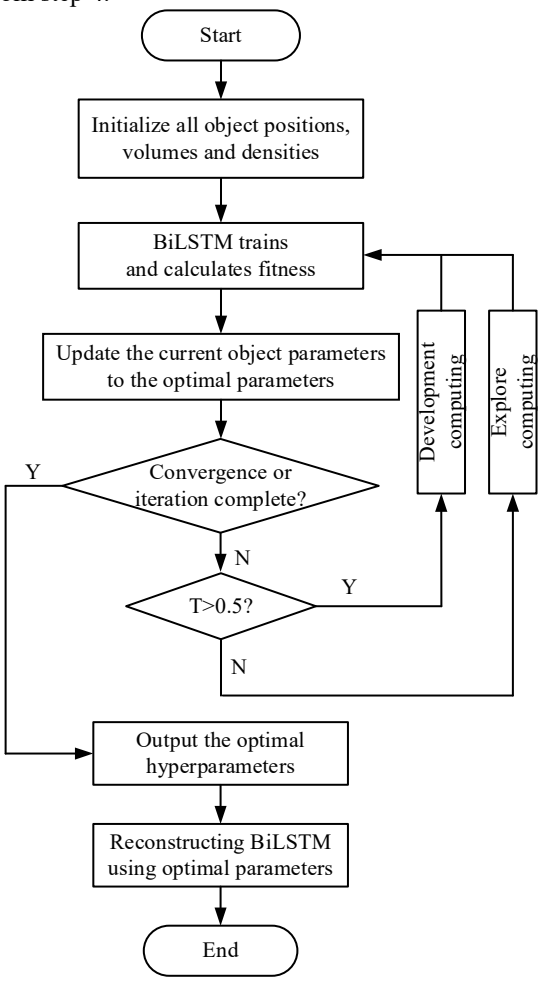

Figure 9. AOA-optimized BiLSTM flow chart

3.7. Power Prediction Model

For power prediction, the expression is shown in equation (25):

$$[\hat{P}^k_{t+1}, \hat{P}^k_{t+2}, \cdots, \hat{P}^k_{t+p}] = f^k_{BiLSTM}\left(P^k_{t-1}, P^k_{t-d+1}, \cdots P^k_t\right) \quad (25)$$

where p and d are the length of the prediction time domain and the length of the input power sequence respectively; f^k_{BiLSTM} is the BiLSTM prediction model corresponding to the k-th component; $P^k_{t-1}, P^k_{t-d+1}, \cdots P^k_t$ and $\hat{P}^k_{t+1}, \hat{P}^k_{t+2}, \cdots \hat{P}^k_{t+p}$ are the prediction input sequence and the prediction result sequence.

4. Predictive EMS Based on Model Predictive Control

Predictive control is characterized by an indeterminate global working condition, which precludes the determination of the global optimal energy allocation. However, rolling optimization enables the identification of a nearly optimal energy allocation. Figure 10 illustrates the architectural components of the MPC-based EMS described in this paper, categorized by sampling moment. The sequence of phases is as follows:

1. Observe the current state of the system, including the SOC of the battery and UC;
2. Apply the power prediction model to forecast the power and determine the power demand during the interval;
3. Determine the optimal control sequence and use DP to solve the optimization problem within the power prediction interval at the current sampling moment; update the system state with the initial element of the sequence;
4. Reiterate steps 1 through 3 immediately thereafter to maintain continuous optimization until the simulation concludes.

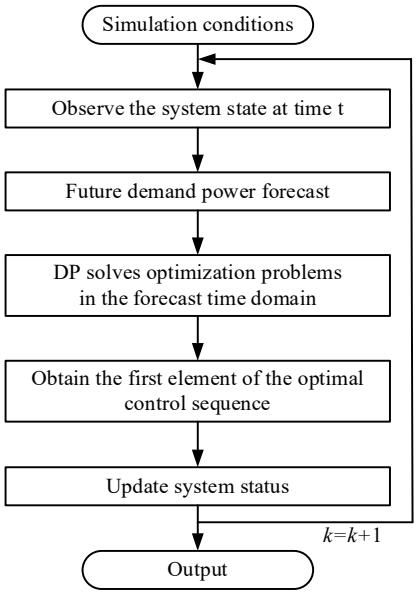

Figure 10. MPC calculation flow chart

The UC SOC is selected as the state variable and P_{DC} as the control variable, and its state transfer equation is as follows:

$$\begin{cases} SOC_{uc}(k+1) = SOC_{uc}(k) + \dot{SOC}_{uc} \cdot \Delta t \\ \dot{SOC}_{uc} = \dfrac{V_{oc\_uc} - \sqrt{V^2_{oc\_uc} - 4R_{uc} \cdot P_{uc}}}{2R_{uc} \cdot V_{oc\_uc} \cdot C_{uc}} \end{cases} \quad (26)$$

where C_{uc} is the rated capacity of the UC; K is the time step; Δt is the sampling time interval.

In the prediction time domain, the system objective function is:

$$J = \min \sum_{t=k}^{k+p} \left[E_{loss}(t) + \varphi\left(SOC_{uc}(t+1)\right) \right] \tag{27}$$

where $\omega(SOC_{uc}(t))$ is the penalty function that constrains the UC SOC from falling below the reference value and has the following expression:

$$\omega\left(SOC_{uc}(t)\right) = \begin{cases} 0, & SOC_{uc}(t) \geq SOC_{uc\_ref}(t) \\ \alpha\left(SOC_{uc}(t) - SOC_{uc\_ref}(t)\right), & SOC_{uc}(t) < SOC_{uc\_ref}(t) \end{cases} \tag{28}$$

where α is the normal number; E_{loss} is the energy loss of the composite electric power system, which consists of the sum of the real-time energy loss of the battery, UC and DC/DC, and the specific expression is as follows:

$$E_{loss}(k) = E_{bat,loss}(k) + E_{uc,loss}(k) + E_{DC/DC,loss}(k) \tag{29}$$

where $E_{bat,loss}$, $E_{uc,loss}$ and $E_{DC/DC,loss}$ are the energy losses of battery, UC and DC/DC respectively. The expressions for calculating the energy loss of each part are as follows:

$$\begin{cases} E_{bat,loss} = {I_{bat}}^2 \cdot R_{bat} \cdot \Delta t \\ E_{uc,loss} = {I_{uc}}^2 \cdot R_{uc} \cdot \Delta t \\ E_{DC/DC,loss} = \left| |P_{uc}| - \left| P_{uc} \cdot \eta_{dcdc}^{sign(P_{uc})} \right| \right| \cdot \Delta t \end{cases} \tag{30}$$

Also, the following system constraints need to be satisfied:

$$\begin{cases} P_{req}(k) = P_{bat}(k) + P_{DC}(k) \\ P_{DC}(k) = P_{uc}(k) \cdot \eta_{DC}^{sign(P_{uc})}(k) \\ P_{bat\_min} \leq P_{bat}(k) \leq P_{bat\_max} \\ P_{DC\_min} \leq P_{DC}(k) \leq P_{DC\_max} \\ P_{uc\_min} \leq P_{uc}(k) \leq P_{uc\_max} \\ SOC_{uc\_min} \leq SOC_{uc}(k) \leq SOC_{uc\_max} \end{cases} \tag{31}$$

where min and max are the minimum and maximum values of the corresponding variables.

5. Ruler-based Control Strategies

In contrast to the strategies based on DP and MPC, a ruler-based strategy is also formulated, as illustrated in Figure 11, and includes the threshold value parameters and corresponding explanations presented in Table 2.

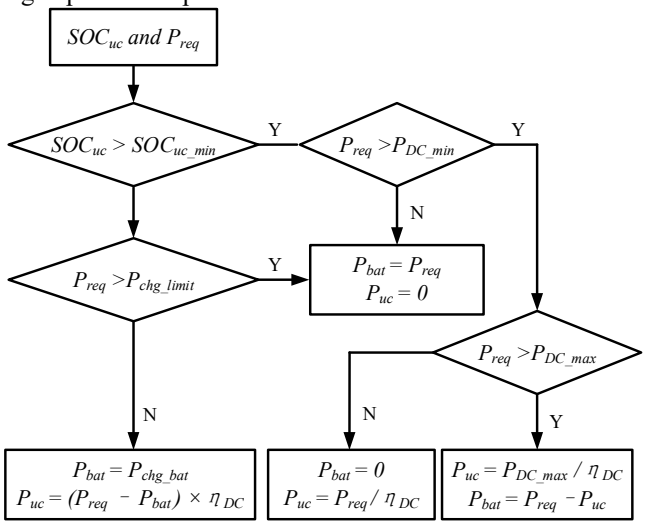

Figure 11. Flowchart of ruler-based EMS

Table 2. threshold parameters of ruler-based strategies

Parameters	Description	Value	Unit
SOC_{uc_min}	Minimum SOC for UC participation in the drive	0.5	-
P_{DC_min}	Minimum DC/DC output power when UC is driven alone	15	kW
P_{DC_max}	Maximum DC/DC output power when UC is driven alone	30	kW
P_{chg_bat}	Battery operating power point in charging mode	20	kW
P_{chg_limit}	Transition to charge mode demand power threshold	10	kW
P_{req}	The request power of motor	-	kW
SOC_{uc}	Current SOC of UC	-	-
η_{DC}	DC/DC efficiency	-	-
P_{bat}	Battery Power	-	kW
P_{uc}	UC Power	-	kW

6. Simulation results analysis

To assess the efficacy of the prediction model and the MPC-based energy management method presented in this study, simulations are conducted using the MATLAB platform. The sampling interval in the predictive control method is configured as 1 second, while the prediction time domain is set to 5 seconds. This configuration allows for consideration of both optimization effects and calculation time. Simultaneously, the beginning values of both the UC and battery are set to 0.75, while the termination reference value for the UC is 0.5. Table 3 displays the primary parameters of the ship's components.

Table 3. threshold parameters of simulation ship

Component	Parameter	Value
Battery	Rated capacity/Ah	100
	Peak power of discharge/kW	40
	Peak power of charge/kW	36
Ultracapacitor	Rated capacity/F	300
	Maximum voltage/V	403
	Peak power of discharge/kW	45
	Peak power of charge/kW	30
DC/DC	Maximum power/kW	40

6.1. Power prediction results and analysis

As depicted in Figure 12 (a), the power data were collected from the motors in the laboratory with simulated working conditions. Figure 12 (b) shows the division of training and test data. Set the number of objects in the AOA to 5 and the maximum number of iterations to 100. The K and α ranges are specified as [2,6] and [0,2000], respectively. The optimal K and α values are determined to be 6 and 4, respectively. Following AOA to VMD optimization in the training set, the minimum envelope entropy is obtained at 7.9812. Based on these settings, the results of AOA optimized VMD are visually represented in Figure 13.

The decomposition results of the training set are displayed in Figure 14. It is evident that the IMF1 amplitude is the highest, closely resembling the original signal, and amplitude of each other IMF gradually decreases. As observed in Figure 14-(b), the IMF1 to IMF4 components, which constitute the main components, exhibit minimal fluctuations and display a strong regular pattern. This regularity is advantageous for the power prediction model to learn the power characteristics. On the other hand, the IMF5 and IMF6 components exhibit significant fluctuations but have relatively small amplitudes. Despite the significant variations in IMF5 and IMF6, the magnitude of the components is minimal, therefore exerting small impacts on the prediction outcomes.

(**a**) Experimental platform

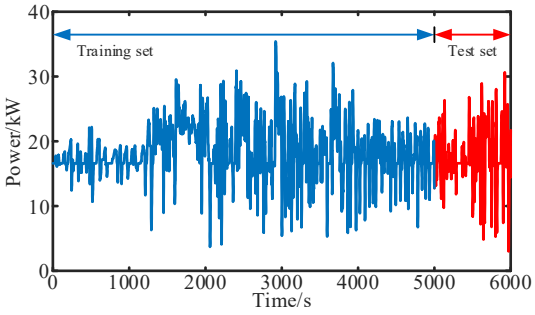

(**b**) Division of training and test set data

Figure 12. Training set and test set data

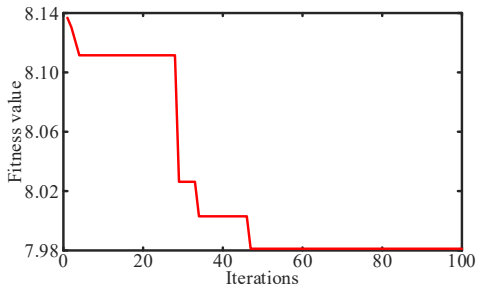

(**a**) Change curve of fitness value

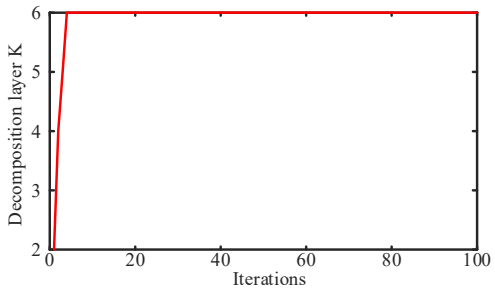

(**b**) Change curve of decomposition layer K

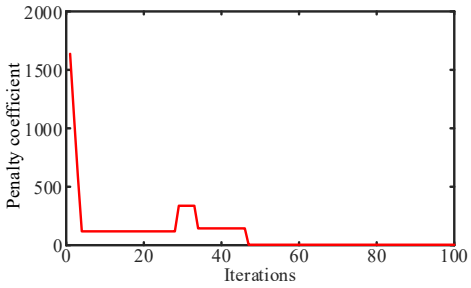

(**c**) Change curve of penalty coefficient α

Figure 13. Results of AOA optimized VMD

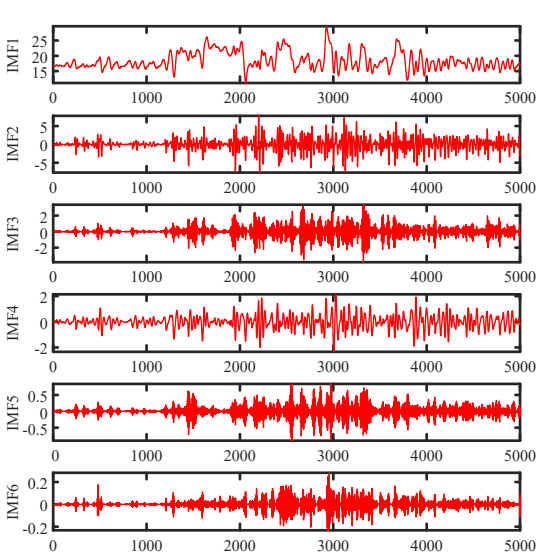

(**a**) Training set decomposition results

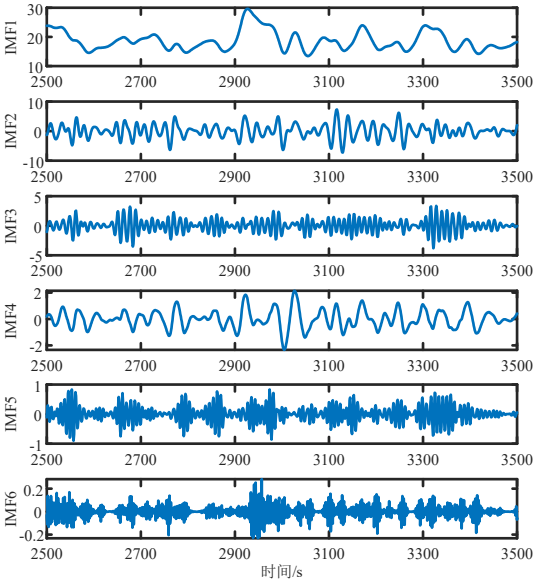

(**b**) Results of 2500s to 3500s decomposition

Figure 14. Results of VMD decomposition for the training set of operational conditions

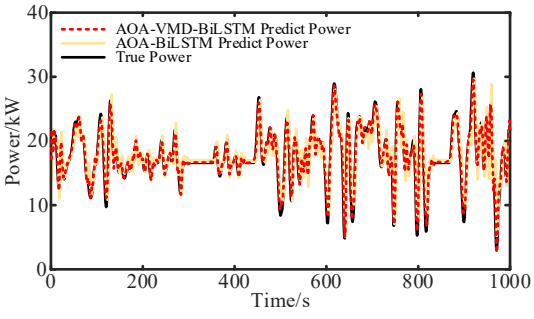

(**a**) Prediction results of two power prediction models

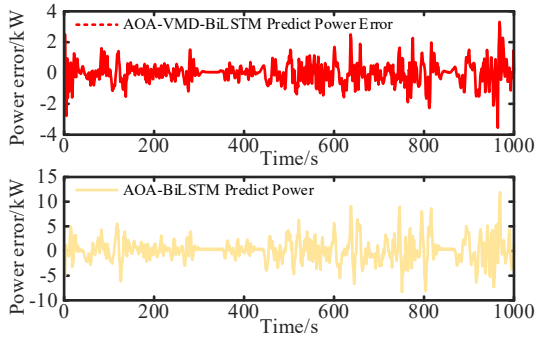

(**b**) Comparison of prediction errors of two prediction models

Figure 15. Results of power prediction

To assess the efficacy of the prediction model developed in this research, it is compared to the AOA-BiLSTM prediction model. The prediction outcomes of both models are depicted in Figure 15. Based on the Figure 15, it is evident that both prediction models exhibit improved accuracy in predicting power. However, the suggested prediction model in this research demonstrates a closer approximation to the genuine value during local power peaks. The power error depicted in Figure 15-(b) indicates that the prediction error of the proposed prediction model in this paper is primarily focused within the range of -2 to 2 kW. This range is significantly smaller compared to the power prediction error of -5 to 5 kW observed in the AOA-BiLSTM model. Additionally, the peak error of the AOA-VMD-BiLSTM model is considerably smaller than that of the AOA-BiLSTM model.

To facilitate a fair comparison of prediction results, the power prediction results are quantitatively evaluated using the Root Mean Squared Error (RMSE) as the evaluation metric. A higher RMSE value indicates lower prediction accuracy. The expression is as follows:

$$\mathrm{RMSE}=\sqrt{\frac{\sum_{k=1}^{N}\sum_{i=1}^{p}\left(P_p(k+i)-P_t(k+i)\right)^2}{N\times p}} \tag{32}$$

where $P_p(k+i)$ and $P_t(k+i)$ are the predicted and true power at i moments after k moments, respectively; p and N are the predicted time domain length and the working condition length.

The RMSE evaluation index of the two prediction models is presented in Table 4. It is evident from the table that the RMSE value of the AOA-VMD-BiLSTM prediction model, proposed in this study, is significantly lower than that of the AOA-BiLSTM model, which serves as the reference benchmark for evaluation. The prediction accuracy has been enhanced by 52.61%, thereby confirming the effectiveness of the proposed prediction model.

Table 4. Power prediction evaluation metrics

Prediction model	Power RMSE/kW	Enhancement of precision/%
AOA-BiLSTM	1.3846	-
AOA-VMD-BiLSTM	0.6561	52.61

6.2. Comparison of MPC simulation results based on two prediction models

Simulations were performed to examine the control effectiveness of the MPC based on two prediction models. The MPC utilizing AOA-VMD-BiLSTM and AOA-BiLSTM power prediction models are referred to as MPC-AOA-VMD-BiLSTM and MPC-AOA-BiLSTM, respectively.

The simulation results of the MPC, which are based on two prediction models, are displayed in Figures 16-18. The figures demonstrate that the SOC variations in the battery and UC are comparable under both MPC strategies, with minor discrepancies. This similarity arises from the fact that the two MPC strategies impose similar constraints on the SOC reference trajectory, resulting in similar discharge patterns and power outputs. Consequently, the SOC variations and energy loss changes are also closely aligned.

The comparison of UC power between the MPC-AOA-VMD-BiLSTM strategy and the MPC-AOA-BiLSTM strategy, as depicted in Figure 19, reveals that both strategies exhibit similar discharging patterns before 600s. After 600s, the range of UC SOC changes becomes small due to the limitations imposed by the reference trajectory. The effectiveness of the control depends on the accurate prediction of power, which varies in accuracy depending on the prediction results. Consequently, this leads to significant differences in control outcomes.

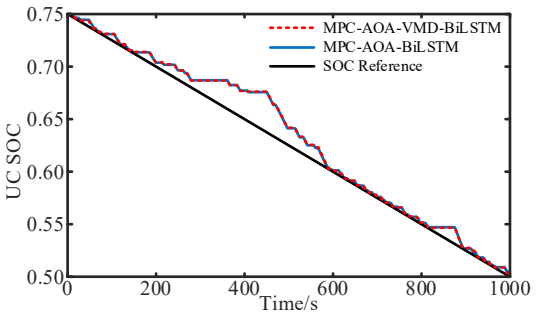

Figure 16. UC SOC variation curves based on two prediction models

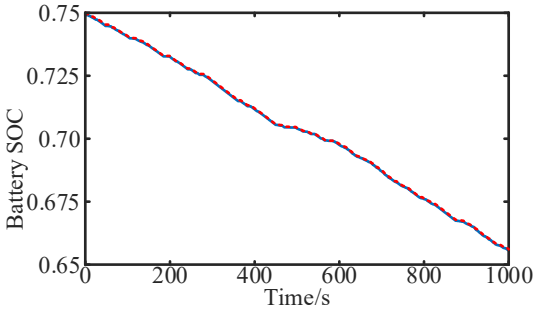

Figure 17. Battery SOC variation curves based on two prediction models

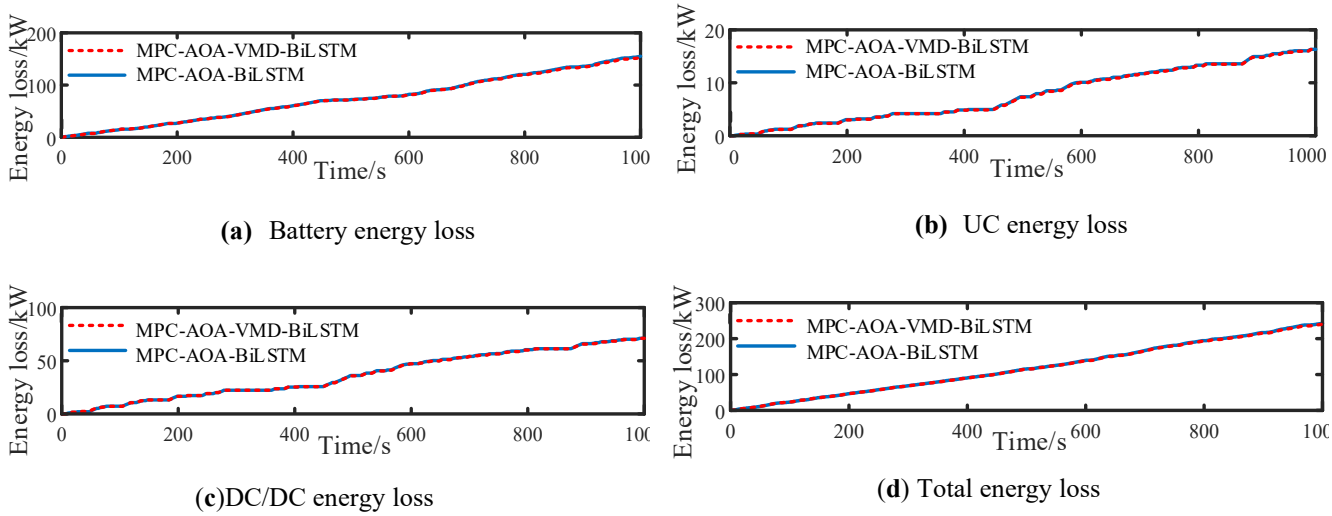

Figure 18. Variation curves of energy loss under two prediction models

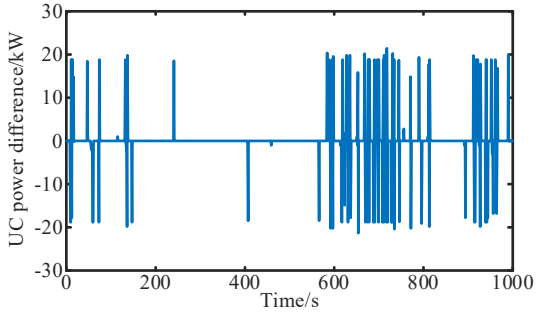

Figure 19. UC power difference under two prediction models

Table 5 presents a comparison of the control effects of two MPC strategies. It is evident from the table that at the conclusion of the simulation, the SOC of the UC and the battery in the MPC-AOA-VMD-BiLSTM strategy are marginally greater than those in the MPC-AOA-BiLSTM strategy. Simultaneously, the energy loss has decreased by 1.02%. This reduction can be attributed to the higher prediction accuracy of the AOA-VMD-BiLSTM power prediction model proposed in this study. The predicted power results closely align with the actual power, enabling more accurate and optimized control variable solutions. The projected power results are closer to the real power, enhancing the accuracy of the control variable solution and boosting the optimization impact. This also demonstrates that enhancing the accuracy of power prediction can enhance the control effect of the MPC method.

Table 5. Comparison of the results of two MPC strategies

Strategy	Ultracapacitor SOC final value	Battery SOC final value	Total energy loss/kW	Energy loss reduction Ratio/%
MPC-AOA-BiLSTM	0.5032	0.6555	243.03	-
MPC-AOA-VMD-BiLSTM	0.5037	0.6558	240.55	1.02

6.3. Comparison of the results of the Ruler, DP and MPC strategies

To assess the efficacy of the integrated prediction model-based predictive EMS presented in this study, it is juxtaposed with the ruler-based and DP-based strategy. The simulation outcomes for each of the three approaches are illustrated in Figures 20-24. The variation curves of the UC SOC (0-300s) and battery SOC as shown in Figure 20 and Figure 21 illustrate that the ruler-based strategy results in a rapid decrease in the UC SOC to 0.5 within 0-300s, followed by fluctuations around 0.5. In contrast, the battery SOC decreases gradually from 0-300s, but accelerates significantly after 300s. In the first 600 seconds, the UC SOC of the DP strategy as a global optimization and the MPC strategy as a local transient optimization exhibit a comparable trend of change. After 600 seconds, the UC SOC returns to its reference trajectory when employing the MPC strategy. However, it remains above the reference trajectory due to significant limitations imposed by the penalty term in the objective function on the extent of its decline. Consequently, the UC SOC fluctuates within a narrow range, which distinguishes it significantly from the UC SOC change observed in the DP strategy.

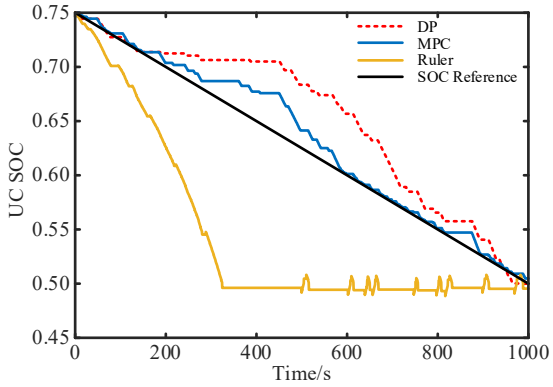

Figure 20. UC SOC Variation Curve

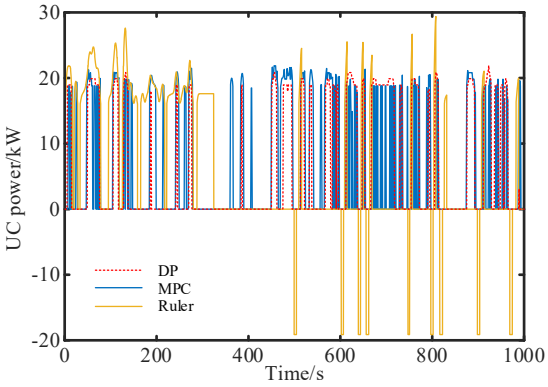

Figure 22. Variation in UC power curve

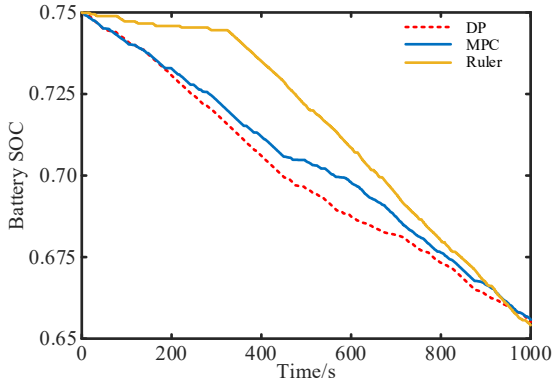

Figure 21. Battery SOC Variation Curve

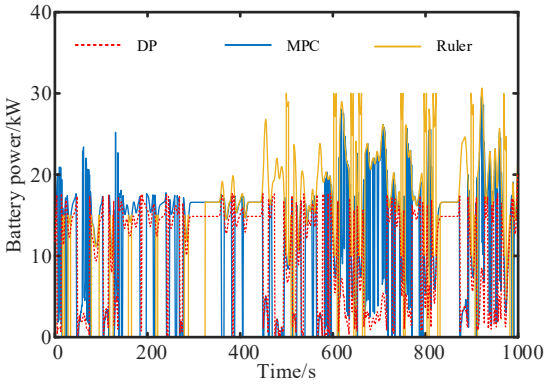

Figure 23. Variation in battery power curve

Figures 22 and 23 depict the power variation curves of the UC and battery. These curves reveal that the UC under ruler-based strategy plays a significant role in the driving work during the first 300 seconds. On the other hand, UC under the DP and MPC strategy is engaged in the middle and high loads, where the required power exceeds 25kW. They operate at approximately 20kW, utilizing a cooperative driving mode for propulsion. After 300 seconds, when the SOC of the UC following a ruler-based strategy falls below 0.5, a portion of the UC power becomes negative to keep the SOC above 0.5. Simultaneously, when the SOC of the UC falls below 0.5, it ceases to contribute to the driving function. Consequently, only the battery drive is utilized, even when there is a high load demand of 30 kW. The variations in UC and battery power changes for the DP and MPC strategies are similar but not identical. This discrepancy can be attributed to three main factors. Firstly, the presence of certain errors in power prediction leads to differences in optimization results. Secondly, the DP strategy aims for global optimization, while the MPC strategy focuses on local optimization search. Lastly, the reference trajectory of UC SOC is not the optimal control trajectory.

Figure 24 illustrates the curve depicting the variation in energy loss. The figure reveals that the ruler-based strategy results in a gradual and slow increase in battery energy loss within the 0-300s timeframe. Conversely, the UC and DC/DC energy loss experience a rapid increase. Beyond 300s, the battery energy loss exhibits a larger increase, while the growth rate of the UC and DC/DC energy loss decreases. This observation aligns with the power change. As a result of the UC's low SOC after 300 seconds, it has minimal involvement in the driving process and is unable to effectively manage the battery's power. Consequently, the battery operates at a higher power level, leading to a quick increase in energy loss. The UC operates within the range of 18-23kW under the DP and MPC methods, primarily focusing on power demands of 25kW or above. This range allows for efficient utilization of the UC and battery power, resulting in reduced energy loss.

The energy losses of the battery, UC, and DC/DC components are higher in the ruler-based strategy compared to the DP and MPC strategies. The energy losses of the DP and MPC strategies are similar to each other. The total energy losses of the ruler-based, MPC, and DP strategies are 285.7Wh, 240.55Wh, and 227Wh, respectively. The DP and

MPC strategies have lower energy losses compared to the ruler-based strategy, with reductions of 20.55% and 15.8%, respectively. Comparing the energy loss of the MPC strategy to that of the DP strategy reveals an increase of only 5.97%, this approximates the global optimal control effect and demonstrates the efficacy of the MPC-based EMS.

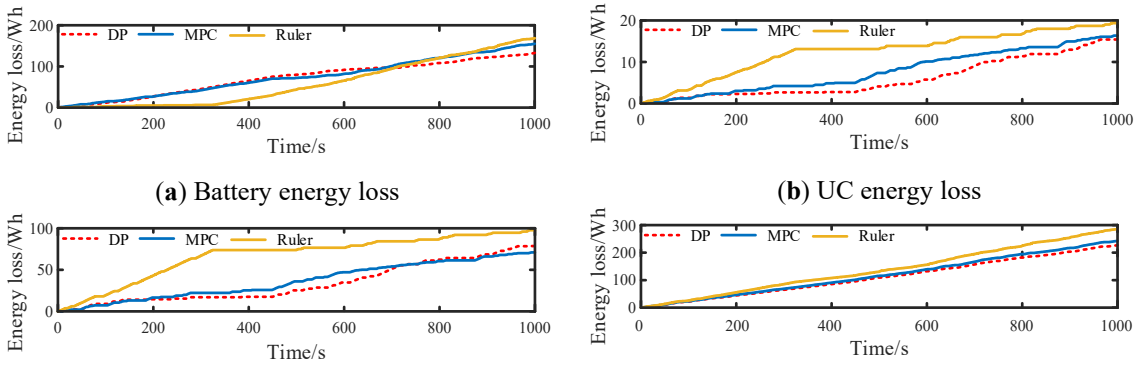

(**a**) Battery energy loss

(**b**) UC energy loss

(**c**) DC/DC energy loss

(**d**) Total energy loss

Figure 24. Energy loss variation curve

7. Conclusions

This work introduces a novel power prediction model that combines AOA optimized VMD with BiLSTM. The purpose is to address the issue of low forecast accuracy caused by the non-stationarity of the power of ship motor. Furthermore, the efficacy of the proposed prediction model is validated using a comparative simulation, resulting in a 52.61% enhancement in prediction accuracy for the combined prediction model compared to the AOA-BiLSTM prediction model under the test scenario. Moreover, the efficacy of the MPC is evaluated by comparing its control effect using two prediction models. The findings suggest that enhancing the accuracy of power prediction can lead to a reduction in energy loss. Ultimately, the EMS based on MPC is contrasted and examined in relation to energy management strategies based on ruler-based and DP approaches. The findings indicate that the MPC method merely increases energy loss by 5.97% compared to the DP strategy but diminishes it by 15.8% in comparison to the ruler-based strategy.

As a result of constraints in experimental conditions, this study presently employs simulation experiments exclusively and not physical experimentation. While this partially substantiates the efficacy of the suggested EMS, there remain disparities when compared to the physical ship during maritime navigation, including hardware charging and discharging limitations and CPU processing speed restrictions. Further research should prioritize the implementation of hardware-in-the-loop systems, in which the controlled components are virtual while the controller is physical, in order to conduct semi-physical simulation experiments. Subsequent investigation into the viability of conducting physical experiments on a larger scale is warranted.

The EMS proposed in this research is not only applicable to maritime ships but also to future vehicles with Level 4 autonomous driving technologies. Level 4 autonomous driving technology is capable of completing driving tasks and monitoring the driving environment under certain specific conditions and environments, which are often characterized by their continuity, stability, and predictability. Therefore, the EMS introduced in this paper can theoretically reduce the energy loss of electric vehicles during these specific working conditions. This could aid in the development of the autonomous driving technology field and also have a positive impact on the new energy vehicle industry.

References

[1] Han, J.G.; Charpentier, J.F.; Tang, T.H. An Energy Management System of a Fuel Cell/Battery Hybrid Boat. ENERGIES 2014, 7, 2799-2820.DOI: 10.3390/en7052799

[2] Halima, N. B.; Hadj, N. B.; Chaieb, M.; Neji, R. Energy Management of Parallel Hybrid Electric Vehicle Based on Fuzzy Logic Control Strategies. J CIRCUIT SYST COMP 2023, 32, 01.DOI: 10.1142/S021812662350007X

[3] Zhang, Z.; Guan, C.; Liu, Z. Real-time optimization energy management strategy for fuel cell hybrid ships considering power sources degradation. IEEE ACCESS 2020, 8, 87046-87059.DOI: 10.1109/ACCESS.2020.2991519

[4] Bukar, A. L.; Tan, C. W. A Review on Stand-alone Photovoltaic-Wind Energy System with Fuel Cell: System Optimization and Energy Management Strategy. J CLEAN PROD 2019, 221, 73-88. DOI: 10.1016/j.jclepro.2019.02.228

[5] Yuan, Y.P.; Wang, J.X.; Yan, X.P.; Shen, B.Y.; Long, T. A review of multi-energy hybrid power system for ships. RENEW SUST ENERG REV 2020, 132, page range. DOI: 10.1016/j.rser.2020.110081

[6] Wilhelm, J.; Janßen, J.; Mergel, J.; Stolten, D. Energy management for a fuel cell/battery hybrid system. Emobility - Electrical Power Train, Leipzig, Germany, 8-9 Nov 2010. DOI: 10.1109/EMOBILITY.2010.5668030

[7] Tang, R.L.; Li, X.; Lai, J.G.; A novel optimal energy-management strategy for a maritime hybrid energy system based on large-scale global optimization. APPL ENERG 2018, 228, 254-264. DOI: 10.1016/j.apenergy.2018.06.092

[8] Zhu, J.Y.; Chen, L.; Wang, X.F.; Yu, L. Bi-level optimal sizing and energy management of hybrid electric propulsion systems. APPL ENERG 2020, 260, 114134. DOI: 10.1016/j.apenergy.2019.114134

[9] Ge, Y.; Zhang, J.; Zhou, K.; Zhu, J.; Wang, Y. Research on Energy Management for Ship Hybrid Power System Based on Adaptive Equivalent Consumption Minimization Strategy. J MAR SCI ENG 2023, 11, 1271. DOI: 10.3390/jmse11071271

[10] Bassam, A.M.; Phillips, A.B.; Turnock, S.R.; Wilson, P.A. Development of a multi-scheme energy management strategy for a hybrid fuel cell driven passenger ship. INT J HYDROGEN ENERG 2017, 42, 623-635.DOI: 10.1016/j.ijhydene.2016.08.209

[11] Lakshmanarao, A.; Kumar, G. V.; Kiran, T. S. R. An Effective Multiple Linear Regression Model for Power Load Prediction. JETIR 2018, 5, 756-760.

[12] Yang, X.Y.; Wang, S.C.; Yan, P.; Chen, J.W.; Meng, L.Z.C. Short-term photovoltaic power prediction with similar-day integrated by BP-AdaBoost based on the Grey-Markov model. ELECTR POW SYST RES 2023, 215, part A. DOI: 10.1016/j.epsr.2022.108966.

[13] Xiang, L.; Liu, J.N.; Yang, X.; Hu, A.J.; Su, H. Ultra-short term wind power prediction applying a novel model named SATCN-LSTM. ENERG CONVERS MANAGE 2022, 252, 115036. DOI: 10.1016/j.enconman.2021.115036

[14] Hu, K.Y.; Wang, L.D.; Li, W.J.; Cao, S.H.; Shen, Y.Y. Forecasting of solar radiation in photovoltaic power station based on ground-based cloud images and BP neural network. IET GENER TRANSM DIS 2022, 16, 333-350.DOI: 10.1049/gtd2.12309

[15] Yan, A.Y.; Gu, J.B.; Mu, Y.H.; Li, J.J.; Jin, S.W.; Wang, A.X. Research on photovoltaic ultra short-term power prediction algorithm based on attention and LSTM. IOP Conference Series: Earth and Environmental Science, Xiamen, China, 17-19 Nov 2020.DOI: 10.1088/1755-1315/675/1/012078

[16] Zhao, H.X.; Zhou, Z.L.; Zhang, P.Z. Forecasting of the Short-Term Electricity Load Based on WOA-BILSTM. INT J PATTERN RECOGN 2023, 37, 11. DOI: 10.1142/S0218001423590188

[17] Putz, D.; Gumhalter, M.; Auer, H. A novel approach to multi-horizon wind power forecasting based on deep neural architecture. RENEW ENERG 2021, 178, 494-505.DOI: 10.1016/j.renene.2021.06.099

[18] Houran, M.A.; Bukhari, S.M.S.; Zafar, M.H.; Mansoor, M.; Chen, W.J. COA-CNN-LSTM: Coati optimization algorithm-based hybrid deep learning model for PV/wind power forecasting in smart grid applications. APPL ENERG 2023, 349, 121638.DOI: 10.1016/j.apenergy.2023.121638

[19] Chen, H.; Zhang, Z.H.; Guan, C.; Gao, H.B. Optimization of sizing and frequency control in battery/supercapacitor hybrid energy storage system for fuel cell ship. ENERGY 2020, 197, 117285.DOI: 10.1016/j.energy.2020.117285

[20] Wang, S.; Ma, H.Y.; Zhang, Y.D.; Li, S.Y.; He, W. Remaining useful life prediction method of lithium-ion batteries is based on variational modal decomposition and deep learning integrated approach. ENERGY 2023, 282, 128984.DOI: 10.1016/j.energy.2023.128984